A Numerical Experiment for the Aeroacoustic Study of Orthogonal Blade/Vortex Interaction

P. Zehner [a,1] , F. Falissard [a] , X. Gloerfelt [b]

a. ONERA - The French Aerospace Lab, F-92322 Châtillon, France
b. Arts et Métiers ParisTech, DynFluid Lab, 151 boulevard de l'Hôpital, 75013 Paris, France

Résumé :

La réponse aéroacoustique de l'interaction orthogonale entre une pale en rotation et un tourbillon isolé est étudiée par simulation numérique. Cette étude, réalisée dans un contexte de réduction du bruit des avions à hélices simples et contra-rotatives, doit permettre de mieux caractériser l'influence de la géométrie de la pale et des propriétés du tourbillon sur le bruit rayonné. L'analyse porte à la fois sur la réponse aérodynamique en champ proche et sur le rayonnement acoustique en champ lointain.

Abstract:

The aeroacoustic response of the orthogonal interaction of a rotating blade with an isolated vortex is studied by means of numerical simulation. This study, carried out in a context of noise reduction of propeller and open rotor powered aircrafts, should allow better characterizing the influence blade geometry and vortex properties on the noise radiated by the interaction. The analysis is performed on the aerodynamic response in the near field and on the noise radiation in the far field.

Keywords: aerodynamics, aeroacoustics, blade vortex interaction, noise

1 Introduction

Propeller and open rotor powered aircrafts exhibit a typical acoustic signature with a highly tonal component. Actually, the acoustic spectrum of such aircrafts is characterized by multiple tones emerging at the fundamental and harmonics of the blade passing frequency. If the airflow seen by the rotor is uniform, the maximum noise is radiated in the vicinity of the plane of rotation. This is usually the case when the propellers or rotors are installed in puller position on the nose of the aircraft or far enough ahead the wing leading edge. If the airflow seen by the rotor is inhomogeneous, the acoustic radiation is strongly modified; the overall noise level is generally higher and the maximum noise is no longer observed in the plane of rotation of the rotor but for upstream or downstream directivity angles. This situation occurs when the rotor is installed in pusher position behind wings, fins or horizontal stabilizers, or behind an upstream rotor in the case of counter-rotating open rotors (CROR). The blades of the rotor then interact with an aerodynamic wake, generated by the upstream fixed or rotating lifting surfaces, mainly composed of a velocity deficit and tip or root vortices. These aerodynamic interactions and the corresponding blade pressure fluctuations result in a dramatic change of the acoustic radiation.

Dedicated studies have been conducted at ONERA in the past years to assess and reduce the noise of single propellers [1, 2] and CRORs [3–5]. For the latter, specific designs have been proposed to reduce interaction noise at low speed by means of passive control of the front rotor wake [6]. The noise reduction resulting from the front rotor wake modification could be improved if the rear rotor was specifically designed to minimize the aeroacoustic response of the blade/wake interaction and especially the blade/vortex interaction which is quasi-orthogonal.

The aerodynamics of the orthogonal blade/vortex interaction (BVI) has been studied in the past with a focus on helicopter main rotor/tail rotor interaction [7]. These experimental and computational studies have shown that orthogonal BVI is a complex phenomenon that depends on many parameters such as vortex convection speed, vortex

[1]Corresponding author, Paul.Zehner@onera.fr

axial and tangential velocities, vortex core size, blade velocity, airfoil thickness... Yet, most computations performed in these studies were carried out considering a rectilinear blade in translation motion and only few experiments were carried out using a rotating blade. The present work relies on a numerical experiment allowing to study the influence of parameters not accounted for in previous studies, *i. e.* blade rotation, blade twist, blade loading, vortex path and vortex characteristics.

2 Numerical experiment

The blade used for the interaction, displayed in Fig. 1, is a rectangular blade with NACA-0002 symmetric airfoil section. The non-dimensional tip radius and chord are respectively equal to $R_t = 1$ and $C = 0.2\,R_t$. The rotation tip Mach number is $M_t = 0.65$ and the infinite upstream Mach number is $M_\infty = 0.25$. The blade is twisted along its leading edge with a twist law chosen so that the kinematic angle of attack at leading edge is zero at any radius. The blade will interact with a columnar vortex with exponential decaying vorticity field and zero circulation [8] that has been used in other studies addressing orthogonal BVI noise by means of analytical methods [9]. Considering the compressible Euler equations with a perfect gas law and a homentropic flow, the non-dimensional velocity, pressure and density fields yielding a stationnary vortex are defined as:

$$\frac{v_\theta}{V_{\max}} = \frac{r}{r_c} e^{(1-r/r_c)}\ ,\ \frac{p}{p_\infty} = \left(1 - \frac{V_{\max}^2}{4}\,\frac{(\gamma-1)}{\gamma}\,\frac{\rho_\infty}{p_\infty}\left(1+\frac{2r}{r_c}\right)e^{2(1-r/r_c)}\right)^{\frac{\gamma}{\gamma-1}} \text{ and } \frac{\rho}{\rho_\infty} = \left(\frac{p}{p_\infty}\right)^{\frac{1}{\gamma}} \quad (1)$$

The vortex maximum tangential velocity, $V_{\max} = 0.25 c_\infty \sqrt{M_t^2 + M_\infty^2}$ with $c_\infty = \sqrt{\gamma p_\infty/\rho_\infty}$ the speed of sound, and the core radius, $r_c = 0.025\,R_t$, are set so as to reproduce a realistic blade/vortex interaction. The radius of impingement of the vortex on the blade, represented in Fig. 1, is located at $r_{\text{BVI}} = 0.9\,R_t$.

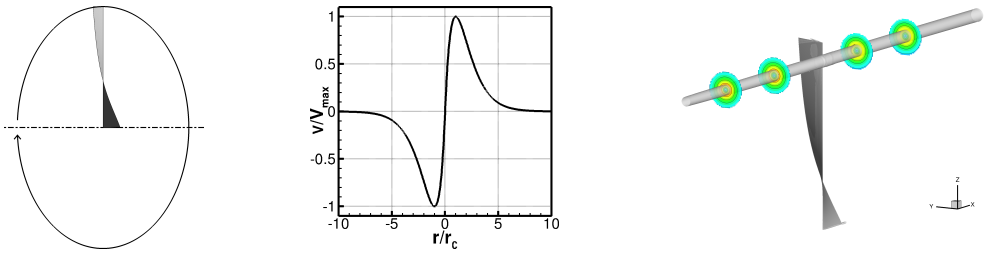

(a) Blade geometry (b) Vortex velocity (c) Blade/vortex interaction

Figure 1: Modeling of the orthogonal blade/vortex interaction

3 Computational Setup

The computational setup used to simulate the aeroacoustic response of the orthogonal interaction of a blade with an isolated vortex is very similar to the one used in Ref. [10]. It is based on the classical chaining of a high-order computational fluid dynamics (CFD) solver with an integral method solver based on the acoustic analogy.

The unsteady aerodynamic flow around the rotating blade is computed by solving the 3D compressible Euler equations with Onera's Cassiopée high-order solver [11, 12] using an automatic off-body overset adaptive Cartesian mesh method based on an octree approach [13]. The computational domain and background Cartesian grids, displayed in Fig. 2, are bounded by a box of dimensions $(x, y, z) \in [-1.4; 3] \times [-3; 3] \times [-3; 3]$. The cell sizes depend on the vicinity to the blade and to the vortex path. The finest cell size, $h_{\min}$, is set so as to have 10 grid points in the vortex core. The near-body mesh discretizing the blade, displayed in Fig. 2, is a two-block O-type mesh composed of 156 cells distributed along the span, 61 cells along the chord, and 51 cells in the normal direction. It has been enhanced compared to the one used in Ref. [10] by regularizing the cell skewness at leading and trailing edges and the cell size in the area of overlapping with the background grid. The unsteady CFD computations use a second-order implicit three-time level backward differencing formula with a time-step corresponding to 0.25 deg of blade motion. The blade motion with respect to the off-body grid is accounted for thanks to the Chimera method [14, 15]. The prescribed vortex and flow condition are set at the upstream boundary by imposing locally the total pressure, the total enthalpy and the direction of the velocity vector. At other boundaries, a classical non-reflecting boundary condition is used.

The noise radiated by the blade/vortex interaction is computed by solving the solid formulation of the Ffowcs-Williams and Hawkings (FWH) equation [16] in the time domain using Onera's KIM code [17] for observer points located on a sphere of radius equal to 20 blade radii.

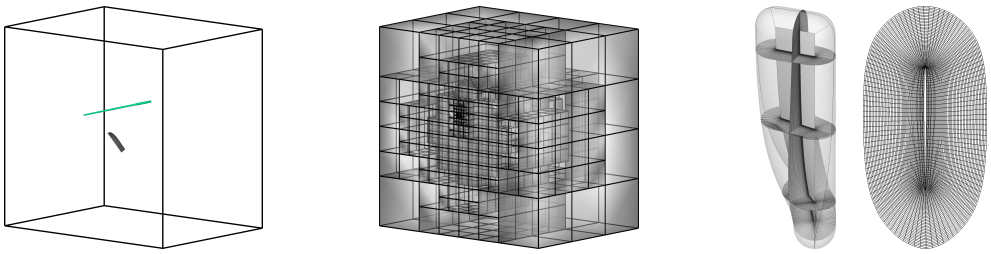

(a) Computational domain (b) Off-body grids (c) Near-body grids

Figure 2: Computational domain, Cartesian off-body grids and near-body curvilinear grids.

4 Results & Discussion

Two unsteady CFD computations have been carried out : one simulating the interaction of the blade with the vortex defined by Eqn. (1), the other simulating the isolated blade. Actually, the blade is twisted so as to have a kinematic angle of attack equal to zero for any radius but three dimensional effects are responsible of a non null thrust. Comparing the two simulations will allow separating the blade/vortex interaction from the stationary component of the flow.

The time-evolution of the thrust coefficient, C_T, defined as $C_T = T/\left(\rho_\infty \left(\Omega/2\pi\right)^2 D^4\right)$, with T the thrust of the blade and D the propeller diameter, is displayed in Fig. 3 for two blade revolutions. Both simulations, with and without vortex, exhibit a non null mean value of thrust coefficient, which is low: 6.85×10^{-3}. We can also see that the first half revolution is affected by a transient evolution of the flow. The interaction between the blade and the vortex is clearly visible around 0 and 360 deg, it is characterized by an impulsive increase and decrease of the thrust with a maximum reached about 4 deg after the theoretical azimuth of impact. Some irregularities are also noticeable near those thrust peaks, in ranges $[-71; 139]$ deg and $[289; 499]$ deg, both for vortex and no vortex simulations. They have been related to the crossing of the near body blade mesh of background grids with different resolutions.

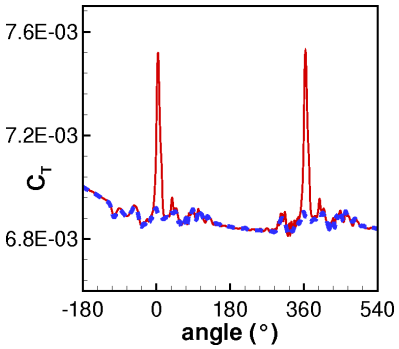

Figure 3: Time-evolution of thrust coefficient with BVI (—), and without BVI (- - -).

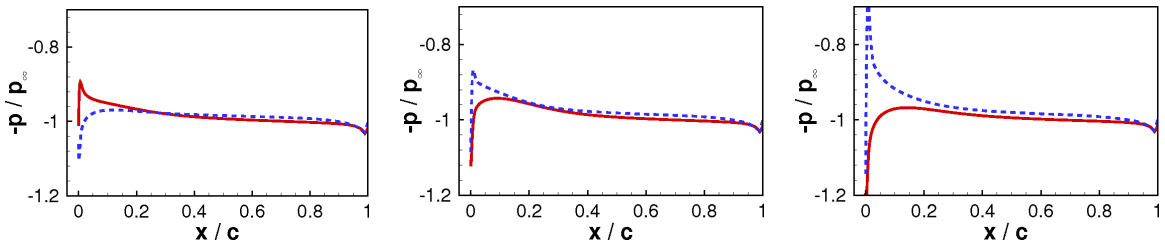

(a) $r = r_{\text{BVI}} + r_c$ (b) $r = r_{\text{BVI}}$ (c) $r = r_{\text{BVI}} - r_c$

Figure 4: Non-dimensional wall pressure on suction side (- - -) and pressure side (—) for three different span locations and blade azimuth of 1 deg.

Chordwise wall pressure distributions are displayed in Fig. 4, for three different blade span locations: $r_{\text{BVI}} + r_c$, r_{BVI} and $r_{\text{BVI}} - r_c$, and for the azimuth of 1 deg, at which wall pressure fluctuations are maximum. High pressure losses take place at blade leading edge, due to the vortex location at that time which generates significant variation of the angle of attack. For span locations corresponding to $r = r_{\text{BVI}}$, and $r = r_{\text{BVI}} - r_c$, the pressure drop is located on the blade suction side, which indicates an increase of the blade thrust at theses locations. On the contrary, at

$r = r_{\mathrm{BVI}} + r_c$ the pressure drop is located on pressure side, which indicates that the blade produces a negative thrust at this location.

The pressure, pressure fluctuation and loading on the blade suction side are plotted in Fig. 5 for a blade azimuth of 1 deg. On these three plots, the main variations are observed at the blade leading edge at radii close to the center of the vortex. The vortex interaction causes a pressure decrease beneath the interaction point r_{BVI} and a pressure increase above. Opposite trends occur on the blade pressure side. The pressure fluctuation has a similar behavior and is almost null at r_{BVI}. The local blade loading, defined as the difference of the pressure on suction and pressure sides, exhibits an increase of thrust for radii lower than r_{BVI}, even far from the vortex core, and a negative thrust for radii higher than r_{BVI}, in good accordance with what was observed on the chordwise pressure distribution displayed in Fig. 4.

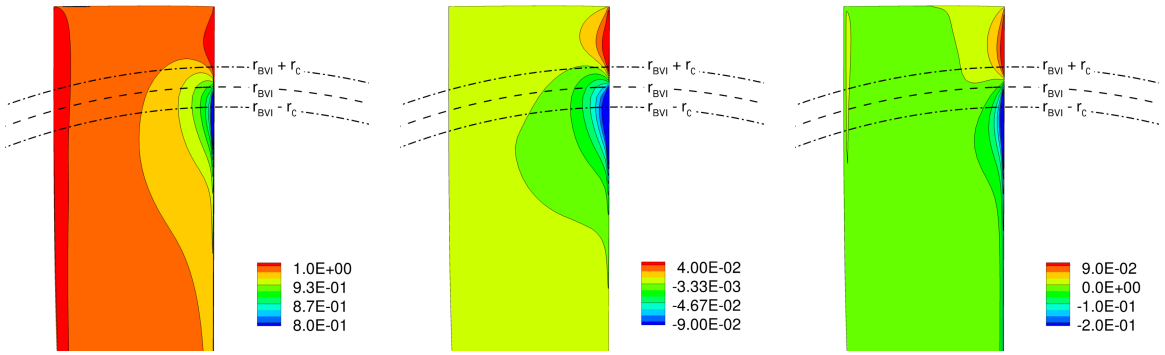

(a) Pressure, $\frac{p}{p_\infty}$ (b) Pressure fluctuation, $\frac{p-p_{180}}{p_\infty}$ (c) Loading, $\frac{p_{\mathrm{suction}}-p_{\mathrm{pressure}}}{p_\infty}$

Figure 5: Pressure, pressure fluctuation and loading on the blade suction side at azimuth 1 deg.

The generation of the acoustic waves resulting from the BVI may be observed through the unsteady pressure fluctuations in the grids attached to the blade. The pressure fluctuation is computed by subtracting the pressure field at 180 deg from the instantaneous pressure field. Slices of pressure fluctuation are presented in Fig. 6 for the blade at azimuth 7deg and different blade span positions: $r_{\mathrm{BVI}} + r_c$, r_{BVI}, $r_{\mathrm{BVI}} - r_c$ and $r_{\mathrm{BVI}} - 2r_c$. This azimuth is selected so as to have fully developed and visible pressure waves. In the figure, the large low pressure zone crossed by the blade corresponds to the pressure loss in the vortex core. Acoustics waves are visible close to the blade leading edge, plotting area is however too narrow to fully seize the wave fronts and directivity in the near field. Wave amplitudes are stronger below the blade vortex interaction radius r_{BVI}.

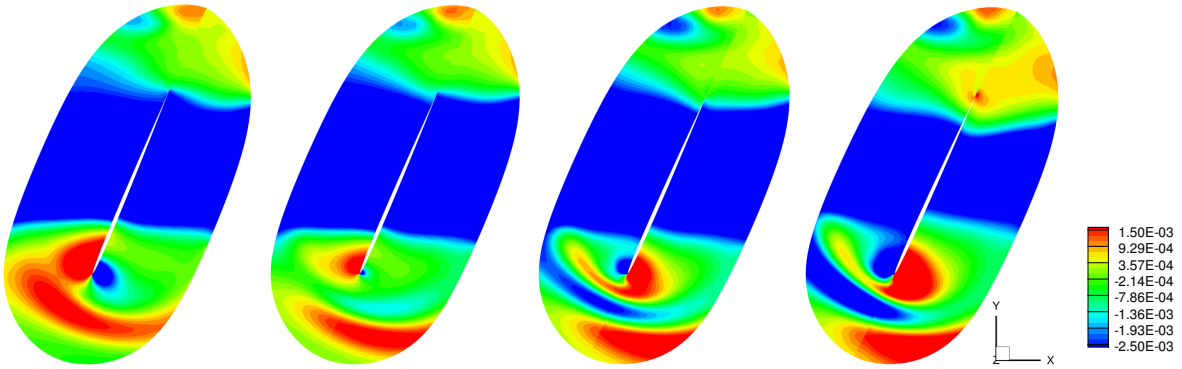

(a) $r_{\mathrm{BVI}} + r_c$ (b) r_{BVI} (c) $r_{\mathrm{BVI}} - r_c$ (d) $r_{\mathrm{BVI}} - 2r_c$

Figure 6: Pressure variation $\frac{p-p_{180}}{p_\infty}$ in different blade span slices at azimuth 7 deg.

As for the CFD computations, two acoustic computations have been carried out using the solid surface formulation of the FWH equation. One for the isolated rotating blade and one for the rotating blade with BVI. Blade thickness noise and blade loading noise are accounted for in these computations. The envelopes of the acoustic spectra computed for the observer points in the far field are plotted Fig. 7, for sound pressure levels (SPLs) expressed in dBs as functions of the blade passing frequency (BPF). The maximum levels, observed at frequencies ranging from $1 \times BPF$ to $10 \times BPF$ are due to the blade thickness noise and blade mean loading noise due to the thrust produced by the blade. Actually, for these low frequencies, the SPLs envelope is the same for the blade with and without BVI. The contribution of the BVI to the maximum radiated noise levels becomes significant for frequencies higher than $10 \times BPF$ and BVI is clearly the main source of the maximum radiated noise levels for frequencies higher than $20 \times BPF$.

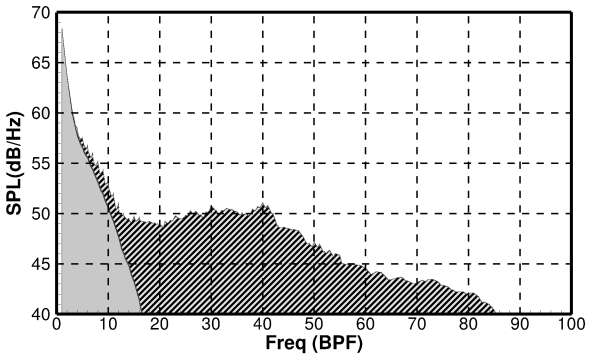

Figure 7: Envelope of the SPLs radiated by the blade with (stripes pattern) and without (plain) BVI.

The Over All Sound Pressure Level (OASPL) and two tones, at frequencies $f = 25 \times BPF$ and $f = 32 \times BPF$, have been selected to study the directivity of the noise radiated by the orthogonal BVI. Those directivities, displayed in Fig. 8, are obtained by subtracting the SPLs radiated by the isolated blade to the SPLs radiated by the blade experiencing BVI. These three-dimensional directivities exhibit a quadrupolar pattern, which was observed in other studies addressing orthogonal BVI noise [9, 10].

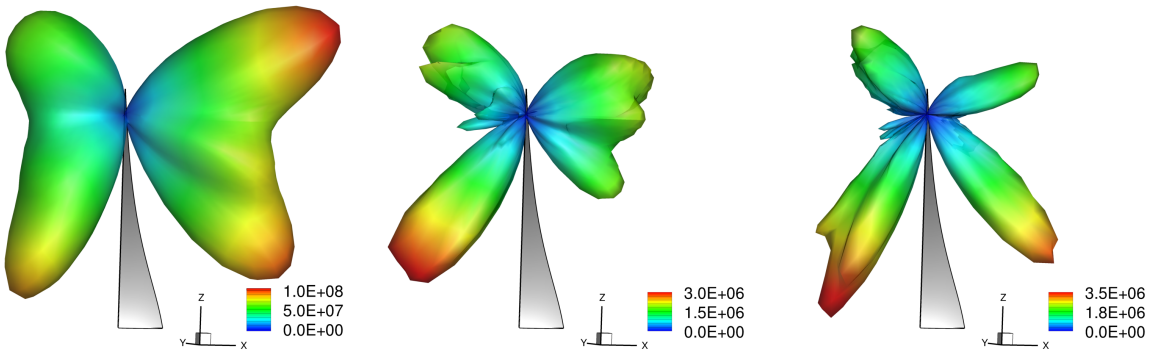

(a) OASPL (b) $f = 25 \times BPF$ (c) $f = 32 \times BPF$

Figure 8: Far field directivity patterns of SPLs, expressed in Pa^2, radiated by the orthogonal BVI.

5 Conclusion

The aeroacoustic response of the orthogonal interaction between a rotating blade and a columnar vortex has been studied by means of computational fluid dynamics and acoustic integral methods. A simplified blade geometry and an analytical vortex model with zero circulation have been used. The discretization of the computational domain

relies on an automatic off-body overset adaptive Cartesian mesh method based on an octree approach. A curvilinear mesh is used to discretize the blade while Cartesian grids with different refinements are used in the background. The unsteady flow simulations are computed using the 3D compressible Euler equations and the noise radiation in the far field is performed using the Ffowcs-Williams and Hawkings equations. Two distinct computations have been made: one for isolated blade and one with blade/vortex interaction. The aerodynamic analysis shows an impulsive increase of the thrust when the blade chops the vortex. It is associated with fluctuation pressure concentrated on the leading edge: negative below the radius of interaction, and positive above. This phenomenon leads to the generation of pressure waves on the suction side and pressure side. The analysis of the farfield acoustic spectra shows that BVI contributes mostly to the SPLs at frequencies greater than $10 \times BPF$. Both OASPL and selected frequency directivities show quadrupoles-like patterns. This numerical setup will be intensively used for analyzing the influence of blade and vortex parameters on the noise radiated by the orthogonal blade/vortex interaction.

References

[1] S. Canard–Caruana, C. Le Tallec, P. Beaumier, and T. Lefebvre. ANIBAL: a new aero-acoustic optimized propeller for light aircraft applications. In *16th AIAA/CEAS Aeroacoustics Conference*, 2010.

[2] A. Giauque, B. Ortun, B. Rodriguez, and B. Caruelle. Numerical error analysis with application to transonic propeller aeroacoustics. *Comput. Fluids*, 69:20–34, 2012.

[3] I. Lepot, M. Leborgne, R. Schnell, J. Yin, G. Delattre, F. Falissard, and J. Talbotec. Aeromechanical optimization of a contra-rotating open rotor and assessment of its aerodynamic and acoustic characteristics. *Proc. Inst. Mech. Eng. Part A - J. Power Energy*, 225:850–863, 2011.

[4] R. Boisard, G. Delattre, and F. Falissard. Computational Fluid Dynamics as a Support to Counter-Rotating Open-Rotor Wind-Tunnel Test Analysis. *J. Aircraft*, 51(2):614–628, 2014.

[5] G. Delattre and F. Falissard. Influence of Torque Ratio on Counter-rotating Open-Rotor Interaction Noise. *AIAA J.*, 2015. doi: http://arc.aiaa.org/doi/abs/10.2514/1.J053797.

[6] G. Delattre, F. Falissard, L. Vion, and L. Jacquin. Open rotor interaction noise reduction through front rotor wake modification. *accepted for publication in Int. J. Aeroacoustics*.

[7] F. N. Coton, J. S. Marshall, R. A. McD. Galbraith, and R. B. Green. Helicopter tail rotor orthogonal blade vortex interaction. *Prog. Aeosp. Sci.*, 40:453–486, 2004.

[8] X. J. Carton and J. C. McWilliams. Barotropic and baroclinic instabilities of axisymmetric vortices in a quasigeostrophic model. In *Mesoscale/synoptic coherent structures in geophysical turbulence*, pages 225–244. 1989.

[9] M. Roger, C. Schram, and S. Moreau. On vortex-airfoil interaction noise including span-end effects, with application to open-rotor aeroacoustics. *Journal of Sound and Vibration*, 333(1):283–306, 2014.

[10] F. Falissard and G. Delattre. Investigation of Counter Rotating Open Rotor Orthogonal Blade/Vortex Interaction Noise. In *20th AIAA/CEAS Aeroacoustics Conference*, 2014.

[11] O. Saunier, S. Péron, G. Jeanfaivre, C. Benoit, and A. Lerat. High-order accurate Cartesian partitioning methods. Application to rotor flows. In *33rd European Rotorcraft Forum*, 2007.

[12] O. Saunier, C. Benoit, G. Jeanfaivre, and A. Lerat. Third-order Cartesian overset mesh adaptation method for solving steady compressible flows. *Int. J. Numer. Methods Fluids*, 57:811–838, 2008.

[13] S. Péron and C. Benoit. Automatic off-body overset adaptive cartesian mesh method based on an octree approach. *J. Comput. Phys.*, 232(1):153–173, 2013.

[14] J.L. Steger, F.C. Dougherty, and J.A. Benek. A Chimera grid scheme. *Advances in Grid Generation, K.N. Ghia and U. Chia, eds., ASME FED*, 5:59–69, 1983.

[15] C. Benoit, G. Jeanfaivre, and E. Canonne. Synthesis of ONERA Chimera method developed in the frame of CHANCE program. *31st European Rotorcraft Forum*, 2005.

[16] J. Ffowcs Williams and D. Hawkings. Sound Generation by Turbulence and Surfaces in Arbitrary Motion. *Philos. Trans. R. Soc. A - Math. Phys. Eng. Sci.*, A264:321–342, 1969.

[17] J. Prieur and G. Rahier. Aeroacoustic integral methods, formulation and efficient numerical implementation. *Aerosp. Sci. Technol.*, 5:457–468, 2001.